

REPORT DOCUMENTATION PAGE

Form Approved OMB NO. 0704-0188

The public reporting burden for this collection of information is estimated to average 1 hour per response, including the time for reviewing instructions, searching existing data sources, gathering and maintaining the data needed, and completing and reviewing the collection of information. Send comments regarding this burden estimate or any other aspect of this collection of information, including suggestions for reducing this burden, to Washington Headquarters Services, Directorate for Information Operations and Reports, 1215 Jefferson Davis Highway, Suite 1204, Arlington VA, 22202-4302. Respondents should be aware that notwithstanding any other provision of law, no person shall be subject to any penalty for failing to comply with a collection of information if it does not display a currently valid OMB control number.  
PLEASE DO NOT RETURN YOUR FORM TO THE ABOVE ADDRESS.

1. REPORT DATE (DD-MM-YYYY) 12-08-2009	2. REPORT TYPE Final Report	3. DATES COVERED (From - To) 1-Jul-2008 - 30-Jun-2009
---	--------------------------------	--

4. TITLE AND SUBTITLE Final report -- NV diamond micro-magnetometer baseline studies	5a. CONTRACT NUMBER W911NF-08-1-0245
	5b. GRANT NUMBER
	5c. PROGRAM ELEMENT NUMBER 7620AN

6. AUTHORS Philip Hemmer	5d. PROJECT NUMBER
	5e. TASK NUMBER
	5f. WORK UNIT NUMBER

7. PERFORMING ORGANIZATION NAMES AND ADDRESSES Texas Engineering Experiment Station Office of Sponsored Research Texas Engineering Experiment Station College Station, TX 77843 -3000	8. PERFORMING ORGANIZATION REPORT NUMBER
---	--

9. SPONSORING/MONITORING AGENCY NAME(S) AND ADDRESS(ES) U.S. Army Research Office P.O. Box 12211 Research Triangle Park, NC 27709-2211	10. SPONSOR/MONITOR'S ACRONYM(S) ARO
	11. SPONSOR/MONITOR'S REPORT NUMBER(S) 54971-PH-DRP.1

12. DISTRIBUTION AVAILABILITY STATEMENT  
Approved for public release; distribution unlimited

13. SUPPLEMENTARY NOTES  
The views, opinions and/or findings contained in this report are those of the author(s) and should not be construed as an official Department of the Army position, policy or decision, unless so designated by other documentation.

14. ABSTRACT  
The goal of this program was to identify applications for which the unique properties of the nitrogen-vacancy (NV) diamond magnetometer gives a significant advantage. Most of the effort concentrated on improving the sensitivity of a single NV to the level where it could be used to detect a single nuclear spin at a distance of 10 nm. Scanning NV nanoprobe development was also explored and significant progress was made.

15. SUBJECT TERMS  
magnetometers diamond nitrogen-vacancy

16. SECURITY CLASSIFICATION OF:			17. LIMITATION OF ABSTRACT SAR	15. NUMBER OF PAGES	19a. NAME OF RESPONSIBLE PERSON Philip Hemmer
a. REPORT U	b. ABSTRACT U	c. THIS PAGE U			19b. TELEPHONE NUMBER 979-845-8932

**Final report**  
**TEES # 32525-A3450**  
**Contract # C08-00977**  
**NV diamond micro-magnetometer baseline studies**

**Summary**

The goal of this program was to identify applications for which the unique properties of the nitrogen-vacancy (NV) diamond magnetometer gives a significant advantage. Most of the effort concentrated on improving the sensitivity of a single NV to the level where it could be used to detect a single nuclear spin at a distance of 10 nm. Scanning NV nanoprobe development was also explored and significant progress was made. Finally some micron-scale full-frame imaging applications such as single neuron imaging were also explored.

**Table of contents:**

Statement of the problem.....	1
Single NV centers as magnetometers.....	2
Isotopically pure diamond.....	6
T <sub>2</sub> * improvement for broadband magnetometry applications .....	9
T <sub>2</sub> improvement beyond environmental magnetic noise.....	10
Vector magnetometry using single NV defect electron spin.....	11
Single NV magnetometers using diamond nanocrystal mounted to AFM tip.....	12
Fabricating diamond nanorods with single NVs.....	14
Enhanced readout using repeated non-demolition read cycles.....	16
Optimizing collection efficiency with plasmon wires.....	18
Full frame imaging magnetometer for single neurons.....	20
Summary of the most important results.....	21

**Statement of the problem:**

The performance of some existing magnetometers is shown in Figure 1. In the ideal case the magnetometer sensitivity scales with the square root of the active volume  $V^{1/2}$  (shot noise limit). For magnetometers based on similar physics, for example magnetic Zeeman shifts this functional dependence might be expected to hold for a variety of magnetometers. Examination of Figure 1 shows that the best magnetometers approximately follow this rule as illustrated by the dashed black line. In general, the goal for magnetic sensing is to be able to detect the field from a single nuclear or electron spin. Since a single spin has a dipole field that falls off a  $1/r^3$  ( $r$  is distance from the dipole) and cannot be closer to the magnetometer than the physical magnetometer size, larger magnetometers must detect weaker magnetic fields to reach the single spin limit. This is illustrated by the dashed blue curves in Figure 1 which decreases as  $1/V$ . Clearly, smaller magnetometer volumes are preferred for single spin detection. In practice, one must also consider standoff range for spin detection and this will determine the smallest magnetometer volume. If we arbitrarily choose a minimum standoff distance of 10 nm corresponding to the minimum volume of  $10^{-24}$  m<sup>3</sup> in Figure 1, then the magnetometer

must detect a field of 1  $\mu\text{T}$  to see a single electron and 1 nT to see a single nucleus. To accomplish this with 1 second of averaging time then requires a magnetometer sensitivity of 1  $\mu\text{T}/\sqrt{\text{Hz}}$  and 1 nT/ $\sqrt{\text{Hz}}$ , respectively.

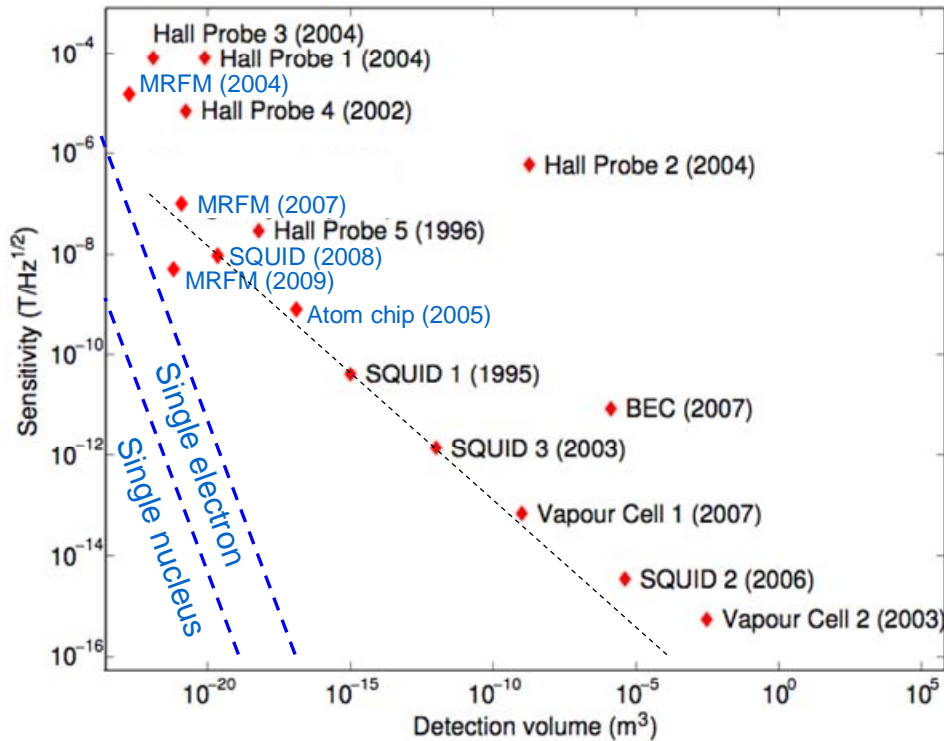


**Figure 1. Comparison of magnetometer technologies. Single electron and nucleus spin detection limits assume dipole magnetic field. The black dashed line drawn as an aid to the eye shows how sensitivity dependence would depend on volume for each magnetometer type in the ideal case of shot noise limit.**

### Single NV centers as magnetometers

The nitrogen-vacancy (NV) color center in diamond is illustrated in Figure 2a. In lightly doped samples, single NVs are readily seen with a confocal fluorescent microscope as shown in Figure 2b. What makes the NV unique is that it can be spin polarized by optical excitation even at room temperature and more importantly that the spin state of a single NV can be read out optically. As shown in Figure 2c, the NV has a triplet ground state and is spin polarized by an intersystem crossing to a metastable singlet state that occurs with 50% probability when the NV is in the  $m = \pm 1$  states and transfers the population to the  $m = 0$  ground state. Spin readout is accomplished by noting that the metastable state has a long lifetime compared to the fluorescence lifetime, so that the average fluorescence is lower for a NV in the  $m = \pm 1$  states. In contrast the  $m = 0$  transition is nominally a cycling transition and does not populate the metastable state. As shown in Figure 2d the resulting difference in fluorescence intensities is relatively large during the optical pumping process, and can be easily detected.

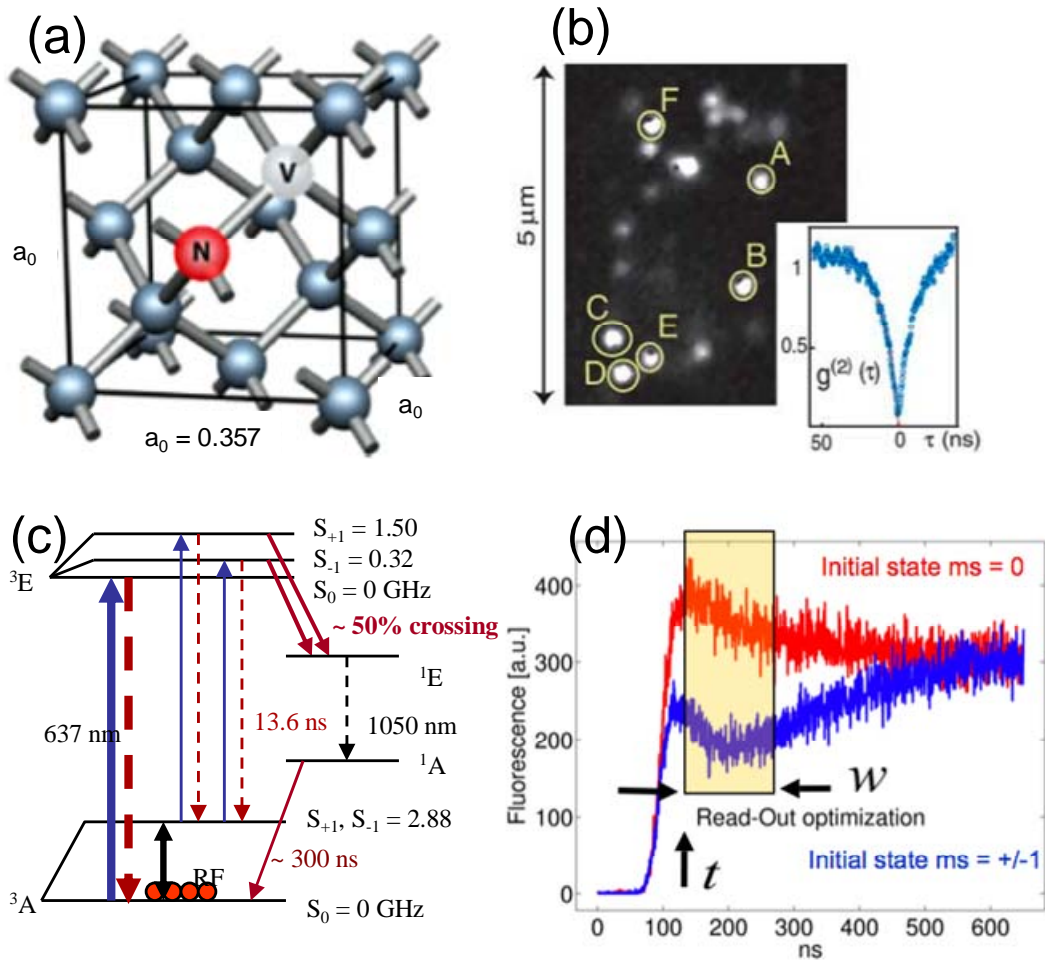


**Figure 2.** (a) The nitrogen-vacancy (NV) color center in diamond consists of a vacancy with adjacent substitutional nitrogen. (b) Fluorescence of individual NVs seen using a confocal microscope. Circled spots were verified to be single emitters by virtue of a photon anti-bunching dip (inset) that goes below 0.5. (c) Energy level structure of NV. The  $m = \pm 1$  excited spin sublevels have 50% probability of crossing over to a single state which eventually decays to the  $m = 0$  state. The  $m = 0$  transition is a cycling transition. (d) Due to the large difference in lifetimes of the excited and metastable states, significantly less fluorescence is emitted from NVs in the  $m = \pm 1$  states before they are pumped into the  $m = 0$  state.

The NV in has a triplet ground state with a total electron spin of 1 and a Zeeman shift of  $\sim 2.8$  MHz/Gauss = 28 MHz/mT. Thus, magnetic fields are measured by monitoring the change in spin transition frequency as illustrated in Figure 3a. The NV has a well defined quantization axis and so the observed frequency shifts will depend on both the magnitude and direction of the magnetic field. For example, if a magnetic field is aligned along the quantization axis then the frequency shifts of the  $m = \pm 1$  transitions will be linear in field strength and symmetric about the zero-field frequency. If the field is not along the quantization axis there will be a quadratic component. From the line splitting and asymmetry of the line shifts it is possible to determine both the magnetic field magnitude and its angle with respect to the quantization axis. Using information from different NV orientation, the absolute B-field orientation can be determined.

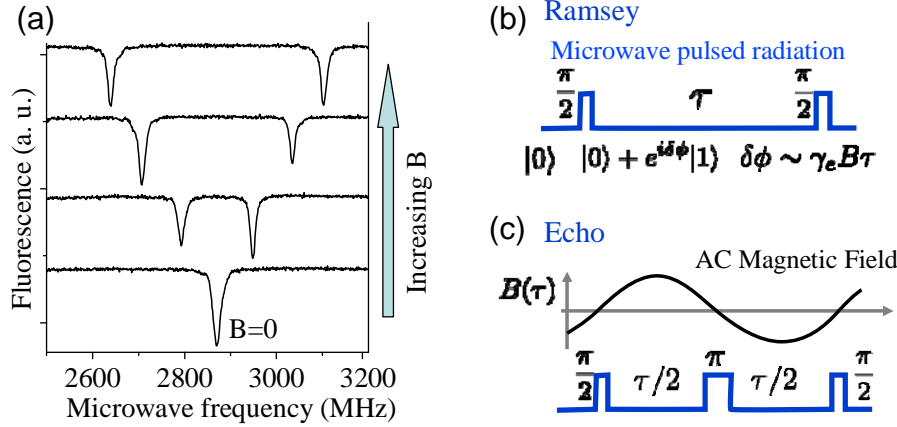


**Figure 3.** (a) Magnetic fields cause Zeeman shifts in the electron spin transitions. The transitions are from the  $m = 0$  to  $m = \pm 1$  ground state sublevels. (b) Ramsey fringe technique overcomes limitations of power broadening and allows detection of rapidly changing fields without loss of sensitivity. (c) Spin echoes cancel out noise from slowly varying or DC magnetic fields such as those produced near the NV by  $^{13}\text{C}$  spins in the diamond lattice.

In analogy to atomic vapor magnetometers, the NV magnetometer sensitivity will be determined by the Zeeman shift divided by the spin transition linewidth, and multiplied by the signal to noise ratio (SNR) of the spin state detection scheme. For single NVs and a well designed experimental setup, the SNR will be shot noise limited up to long averaging times. The linewidth is determined by a number of factors. For example the cw spectrum of Figure 3a has a linewidth which includes power broadening from both the microwave and optical fields. Rapidly changing magnetic fields also broaden the cw spectrum but this can usually be de-convolved to retrieve the frequency spectrum of the magnetic field. Power broadening can be eliminated by using Ramsey fringe excitation as shown in Figure 3b. Here the microwave field that drives the spin transition is split into pairs of pulses. The second pulse of each pair creates an interference that varies as the accumulated phase shift which in turn depends on the pulse time separation  $\tau$  and the Zeeman shift. Taking the appropriate wavelet transform of the interference signal vs  $\tau$  retrieves the magnetic field as a function of time.

For both cw and Ramsey fringe techniques the limiting magnetic sensitivity is determined the ensemble-averaged linewidth  $1/T_2^*$ . Even for single NV the ensemble limit applies unless the signal can be detected in a single shot, which currently is not possible. To overcome the  $T_2^*$  limit, spin echoes can be used as shown in Figure 3c. Here the phase shift accumulated between the first pair of pulses is exactly canceled by that accumulated over the second pair. This cancellation is not complete if the magnetic field changes significantly during the pulse sequence. Maximum sensitivity is achieved when the magnetic field is synchronized with the pulse sequence as illustrated in Figure 3c. In this case the magnetic sensitivity is determined by the spin homogeneous linewidth  $1/T_2$  which is a measure of the spin linewidth for short time scales on the order of a single shot, even though the data can be acquired as an average over many shots.

When we do echo spectroscopy on single NV centers in the absence of an external fluctuating field we find that the signal instead of decaying exponentially for times longer

than  $T_2$ , instead collapses and revives as shown in Figure 4 at a rate that depends on the strength of the applied dc magnetic field. The revivals are only seen in clean diamond with nitrogen concentrations  $\sim$ ppb and are caused by  $^{13}\text{C}$  atoms. Natural diamond is mostly  $^{12}\text{C}$  which is spin-free, and therefore gives the NV its relatively long room temperature coherence time  $T_2$ . However natural carbon also has 1% of  $^{13}\text{C}$  isotopes which have nuclear spin  $1/2$ , and provide a nuclear spin bath. The collapses and revivals can be understood from the perspective of magnetometry. The  $^{13}\text{C}$  in the nuclear spin bath precess at the Larmor frequency providing a local magnetic field at the NV position which changes at this frequency. Since the phase of this field is random every time we run the experiment, revivals exist only when the  $^{13}\text{C}$  atoms complete a full precession on each half of the spin echo sequence. We have detected revivals up to 1 ms coherence time. Thus, remarkably by tuning to a revival peak we can undo the evolution of the environment and be sensitive now to external oscillating magnetic fields.

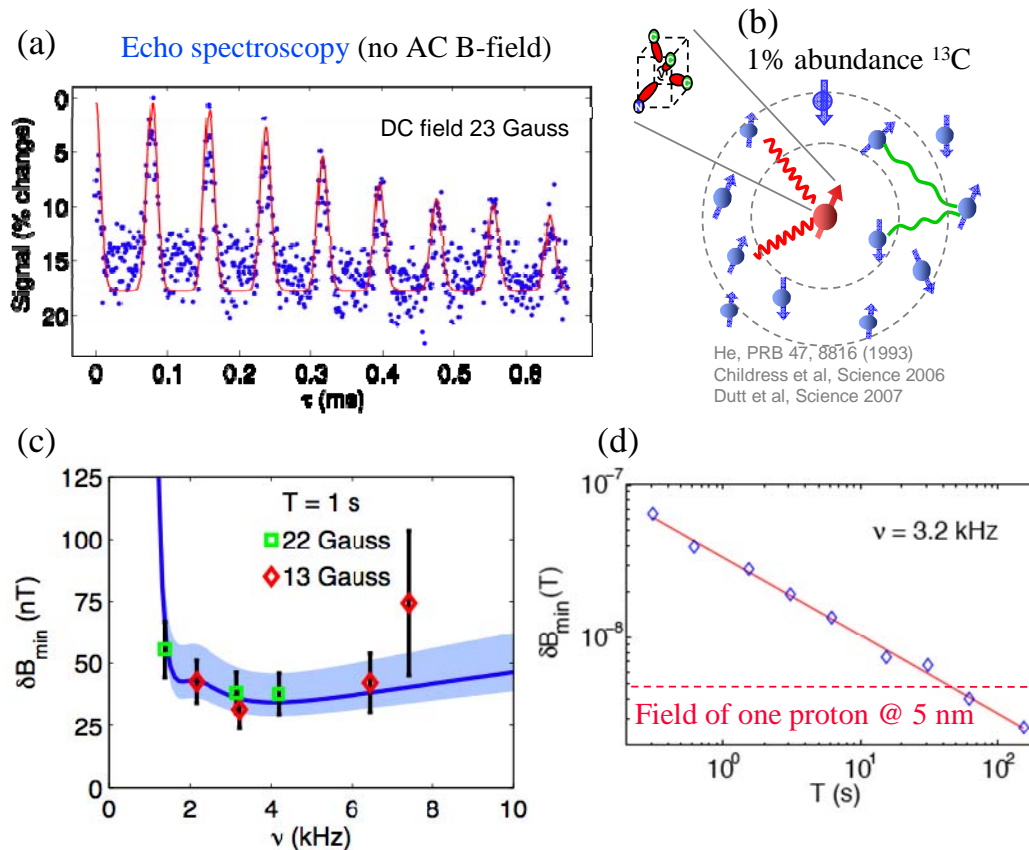


Figure 4. (a) Experimental spin echo with no applied ac magnetic field. The revivals are due to Larmor precession of the  $^{13}\text{C}$  in the diamond lattice. (b) The  $^{13}\text{C}$  atoms are 1% abundant in natural carbon and ultimately limit the sensitivity of the NV magnetometer. (c) The sensitivity of the NV magnetometer depends the frequency of the magnetic field with a maximum sensitivity in the kHz range. (d) The measured magnetic sensitivity of a single NV compared to the field of a single proton at a distance of 10 nm.

In the Figure 4c we explore the sensitivity for different frequencies of the external magnetic field. For low frequencies, the sensitivity is limited by decoherence which reduces the contrast of the signal. On the other hand, at high frequencies, the sensitivity is limited by the signal bandwidth which broadens the effective spin linewidth. However

the faster signal bandwidth allows a faster pulse repetition rate and in the shot noise limit this improves the SNR a factor proportional to the square root of the signal bandwidth, leading to a net magnetic sensitivity that only goes inversely proportional to the square root of the signal bandwidth. In our experiments, NV centers are more sensitive in the kHz range which is basically the inverse of the coherence time  $T_2$ .

Of course, the more we average, the better we can discriminate the magnetic signal. The minimum field that we can discriminate goes as the inverse square root of the integration time. The more time we spend measuring the signal the better the magnetic sensitivity. This is shown in Figure 4d. Our measurements agree very well with theoretical predictions based on photon shot noise. And the square root dependence on the averaging time indicates that our measurements are shot noise limited up to 100 s of averaging. After 60 seconds of averaging the sensitivity is enough to resolve the field emanated from one proton at 10 nm away.

### **Isotopically pure diamond**

Solid state technologies exploring quantum physics require dedicated types of materials. While classical semiconductor materials have had more than 5 decades of development with respect to purity and structure, carbon based materials are a relatively new class of substances to this field. Since spins are prominent solid state quantum system, research on carbon systems, like, fullerene, nanotubes, graphene or recently diamond is often driven by the requirements of having a spin-free lattice. The most abundant isotope of carbon,  $^{12}\text{C}$  (98.9%) is nuclear spin free. Thus, carbon materials are among a limited family of substances (including Si and Ge) which can be engineered to contain a very low level of nuclear spins, in contrast to GaAs, for example. Diamond's recently reported long phase memory and relaxation times as a result of the low natural spin abundance<sup>6</sup>, makes it ideally suited for high sensitivity applications such as magnetometry.

The single crystal diamond samples studied here were synthesized with a microwave plasma-assisted CVD reactor operating at a frequency of 2.45 GHz. Homoepitaxial CVD diamond layers were deposited onto specially prepared  $\langle 100 \rangle$  oriented diamond substrates. Care was taken to ensure that the surface quality of the substrates was as high as possible to minimize the dislocations in the epitaxial layer. The challenge in achieving isotopic enriched diamond is to reduce the incorporation of other paramagnetic impurities while using isotopically purified starting material. Isotopic enrichment was accomplished by using purifiers to reduce non-intentional dopants and isotopically enriched methane at 99.7% in a hydrogen environment (95% by composition). These conditions led to samples where the paramagnetic impurity concentration (including nitrogen, hydrogen and silicon defects) was minimized. Intrinsic nitrogen can recombine with vacancies during the growth process with a yield of a few percent leading to formation of nitrogen-vacancy centres in concentration suitable for single centre selection using standard confocal microscopy. By counting single defects in a confocal plane we estimate the concentration of NV defects to be on the order of  $10^{10} \text{ cm}^{-3}$ . By using a rough estimate for the nitrogen to nitrogen-vacancy conversion ratio of one percent, this gives an approximate value for nitrogen impurity concentration of  $5 \times 10^{-2}$  ppb (below the detection

threshold of conventional ensemble spin resonance methods or other bulk techniques such as SIMS).

At such a low concentration of paramagnetic impurities, ultrapure CVD diamond has the potential to become a new class of material where electron single spins could be observed at room temperature at distances up to hundreds of nanometres. Ordinarily, a single impurity spin in a lattice will usually lose its phase quickly, due to interaction with other spins and phonons. However in diamond, owing to strong binding between low-mass carbon atoms, phonon limited spin lattice relaxation times are as long as  $10^2$  to  $10^4$ s. This means that the phase coherence time of electron spins in room temperature diamond is not limited by spin-lattice interactions (as is the case in other materials), but rather governed by dipolar interactions with other spins. Dipolar coupling to other electron spins can be neglected in this ultrapure material because of the large distances to neighbouring nitrogen impurities (a few microns for the estimated  $10^{-2}$  ppb concentration). Hence the main source of electron spin decoherence is the nuclear spin bath arising from the presence of  $^{13}\text{C}$  atoms.

To exemplify this effect we show the electron spin resonance linewidth of a single NV defect centre as a function of  $^{13}\text{C}$  concentration (Figure 5). Spectra recorded by acquiring the free induction signal (FID) of the single electron spin, Figure 5a, show that as the  $^{13}\text{C}$  nuclear spin concentration is diminished, the electron spin inhomogeneous decay rate  $T_2^*$  is drastically reduced, acquiring a comparatively long FID decay time of tens of microseconds. Taking the FFT, the full width half maximum spin linewidths are shown in Figure 5b. In isotopically enriched NV diamond the  $T_2^*$  width is 55 kHz which is the smallest single electron spin resonance linewidth ever measured in a solid state material.

The full width half maximum of the electron spin resonance line of a single defect is related to the  $^{13}\text{C}$  concentration by  $\delta = \frac{2}{\pi} \sqrt{2M_2}$  where  $M_2 \propto \frac{1}{5} f \gamma_c^2 \hbar^2 \sum_k r_k^{-6}$  and the summation is over all  $^{13}\text{C}$  nuclei,  $f$  is the abundance of  $^{13}\text{C}$  nuclei and  $\gamma$  is nuclear spin gyromagnetic ratio. From this we can estimate the abundance of  $^{13}\text{C}$  as measured by electron spin resonance to be 0.5 % which is in qualitative agreement with the concentration of  $^{13}\text{C}$  impurities in the enriched methane used for the diamond growth (0.3 %).

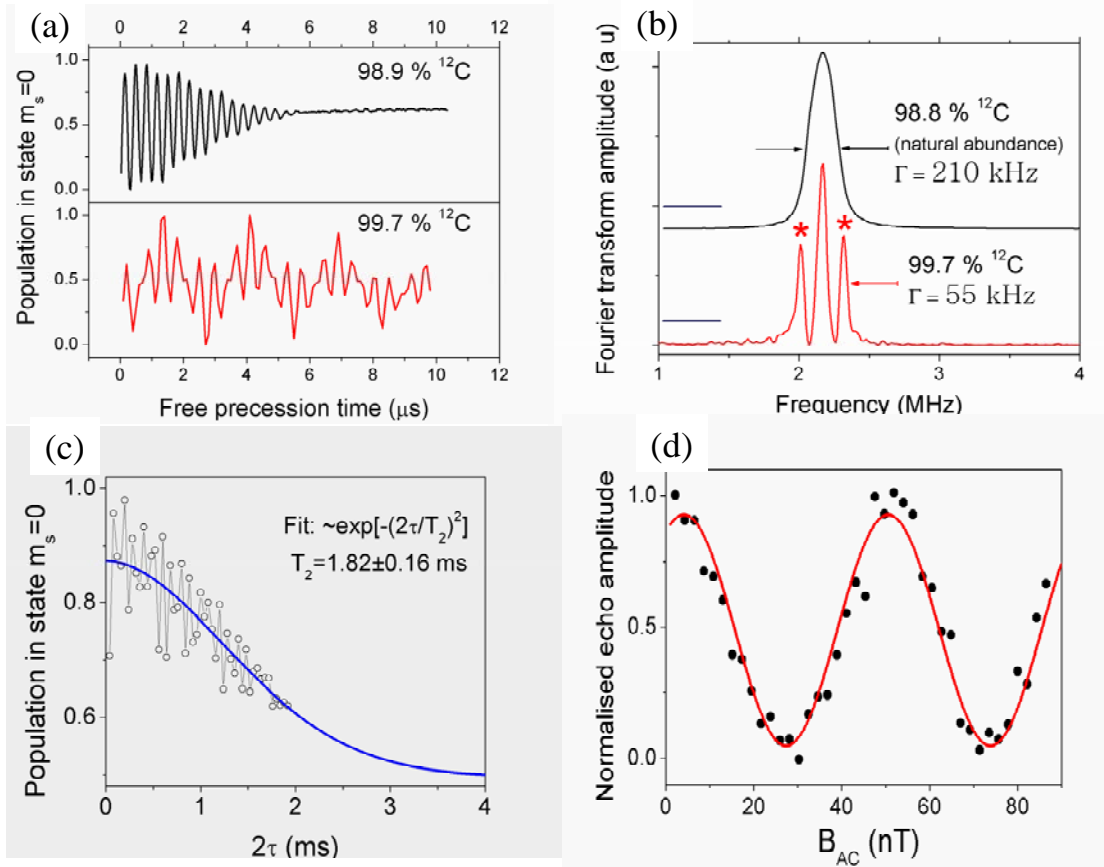


**Figure 5.** (a) Free induction decay (Ramsey) signal measured on a single NV electron spin for diamond with a natural abundance of  $^{13}\text{C}$  isotope (black curve,  $^{12}\text{C}$  content 0.989) and isotopically engineered crystal (red curve,  $^{12}\text{C}$  concentration 0.997). The applied magnetic field was 690 Gauss. (b) Fourier transform spectra of free induction decay signal. Satellites indicated by arrows are related to the hyperfine interaction with a single  $^{13}\text{C}$  carbon nucleus near the NV. Note that only one out of the three hyperfine components associated with  $^{14}\text{N}$  nuclei of NV defect are present in the spectral range displayed. (c) Spin coherence time for echoes of single spins in isotopically engineered diamond as measured by the decay of spin echo as a function of inter pulse distance. (d) Experimental data on the phase accumulation of the electron spin induction signal upon increase of the external magnetic field strength. The error for the fit function corresponds to a sensitivity of  $4\text{nT}/\sqrt{\text{Hz}}$ .

The low “intrinsic spin noise” of the ultrapure diamond material renders the NV defect to be a sensitive detector for external magnetic fields. Owing to its atomic size, such a NV magnetic field sensor would provide unprecedented performance, both, in sensitivity (i.e.  $\Delta B\sqrt{t}$  where  $\Delta B$  is detectable change of magnetic field within time  $t$ ) and in spatial resolution. From the NV magnetic Zeeman shift of  $h\nu = g\mu_B B_0$ , where  $B_0$  is the external magnetic field, a field of only  $20\text{ mG} = 2\ \mu\text{T}$  would be detectable as a line shift of a  $50\text{ kHz}$  line. This could measure the magnetic field of a single electron at a distance of  $5\text{ nm}$ .

As discussed earlier, the maximum B field sensitivity is achieved in an AC magnetic field changing its sign at time  $\tau$  when the refocusing pulse of an echo sequence is applied. In

this case the sensitivity is given by  $\Delta B = \frac{\pi\hbar}{g\mu_B\sqrt{T_2}}$ , for a total measurement time giving a

SNR of one. The improvement in sensitivity over the FID case arises from increasing the interrogation time from  $T_2^*$  to  $T_2$ . As shown in Figure 5c, the echo coherence time  $T_2$  is  $\sim 1.8$  ms which corresponds to an exceptionally narrow homogeneous linewidth of  $\Delta\nu = \frac{1}{\pi T_2} = 180$  Hz. The corresponding echo amplitude vs AC magnetic field strength is

shown in Figure 5d. A sinusoidal response is obtained because the magnetic field contributes to the overall phase of the coherence and the interference which produces the echo is periodic in this phase.

$$\Delta\phi = \frac{g\mu_B}{\hbar} \int_0^\tau B(\tau) dt$$

The magnetic sensitivity of this measurement is found to be 4.3 nT/ $\sqrt{\text{Hz}}$ , which is high enough to detect the magnetic field of a single nucleus at a distance of just over 5 nm.

The ability of ultrapure isotopically controlled CVD diamond to detect weak magnetic fields with high local resolution might have implications in e.g. life science. An example of which are using diamond magnetometers to detect magnetic fields associated with the ion flow through membrane channels in cells. Another example, owing to their coherent dipolar coupling, is to create an array of NV centres which would present an intriguing room temperature quantum device for quantum computing applications, simulation of phase transitions etc. For such a device the spacing between NV centres can be estimated by considering that the magnetic field created by a single NV spin which is given by

$$B_{dip} = \sqrt{2} \frac{\mu_0\mu}{4\pi} \frac{\sqrt{3\cos^2\vartheta+1}}{r^3} \text{ where } \mu \text{ is the magnetic moment of a single electron spin.}$$

On substitution of the relevant values for  $\mu = 10^{-23}$  JT $^{-1}$  a field of  $10^{-9}$  T is produced by a single NV spin at a distance of roughly 100nm. Using this value we conclude that with the current limit in dephasing times, two NV electron spins, at a distance of 100nm, will be coherently coupled. This distance is sufficient for the two centres to be addressed and read out separately by modern methods of non-linear optical microscopy and also manufacturable with current implantation techniques that allow some 10nm precision.

### **$T_2^*$ improvement for broadband magnetometry applications**

Although the longer coherence time achieved by reducing the concentration of  $^{13}\text{C}$  in the diamond lattice meets the main goal originally chosen for this research, the more important result for most applications is actually the much longer  $T_2^*$  coherence lifetime. This is because the echo technique is restricted to detecting only periodic magnetic signals that are phase locked to the echo pulse sequence, whereas the Ramsey fringe, or FID, technique can detect magnetic fields with arbitrary time dependence.

Figure 6 shows a demonstration of such a time-domain magnetic field measurement. As shown in Figure 6a a magnetic test signal is applied between the two microwave pulses of a Ramsey fringe sequence. Initially  $\tau$  is chosen such that the fluorescence corresponds to maximum amplitude of the Ramsey fringes, thus matching the minimum detection

bandwidth to that of the signal. Switching on the test magnetic field  $B(t)$  for various lengths of time during the free precession interval causes oscillations of the readout signal, as shown in Figure 6b, indicating an accumulation  $\Delta\phi$  as described earlier. A wavelet transform recovers the time variation of the magnetic field (see Figure 6c).

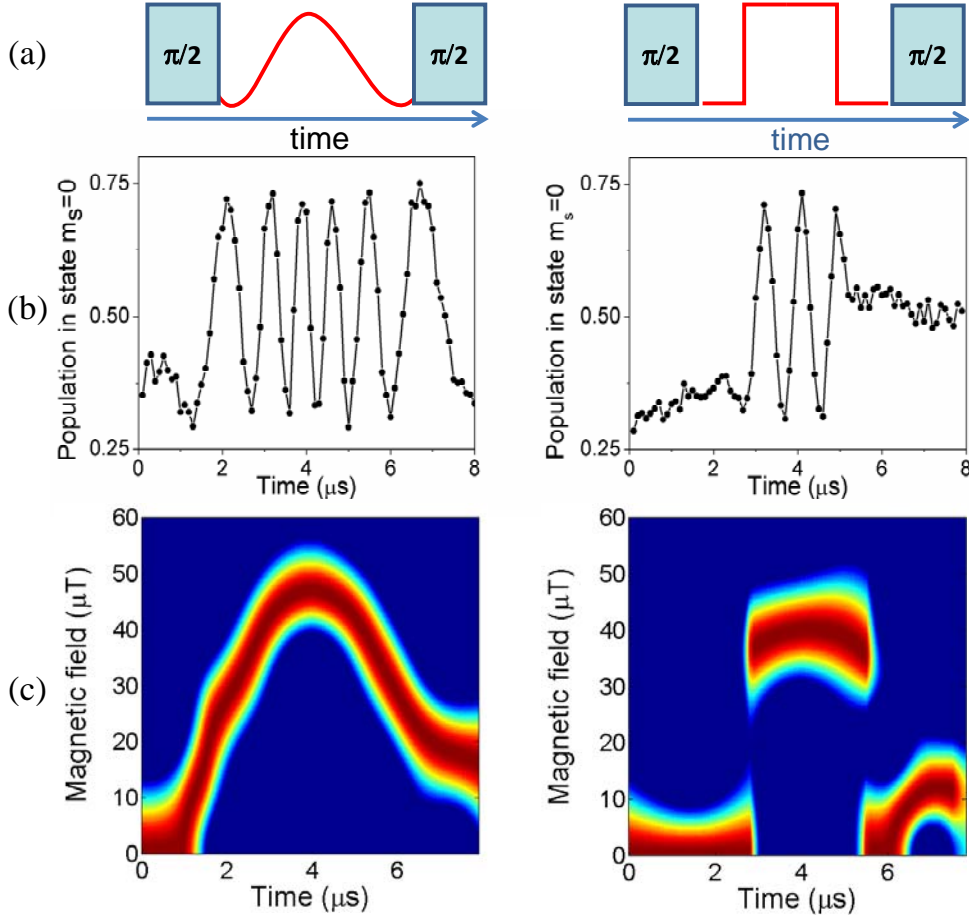
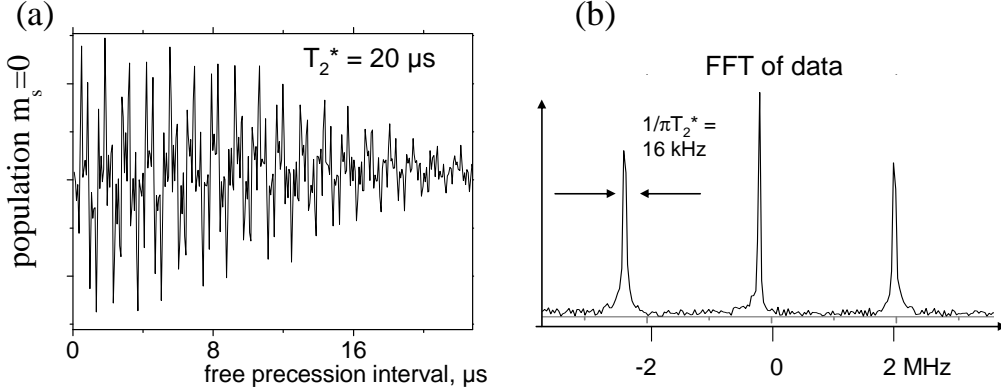


Figure 6. (a) Ramsey fringe pulse sequence used to time arbitrary dependent magnetic fields using single NV spins in isotopically enriched diamond. The two test patterns presented are a sine wave (left) and a square pulse (right). (b) Experimental data showing accumulation of the phase of the free induction decay resulting from the respective applied magnetic field. (c) Reconstructed magnetic field time profile showing agreement of the reconstructed time dependence of the magnetic signal to its actual time dependence.

### **$T_2$ improvement beyond environmental magnetic noise**

The ultimate limit of coherence time for spin-free diamond host is given by spin-lattice relaxation which is expected to occur in a seconds timescale. Thus, further improving the isotopic purity is expected to show even better magnetic sensitivity. This is shown in Figure 7 for diamond with  $\sim 99.99\%$   $^{12}\text{C}$ . As seen in Figure 7a the coherence time is now much longer giving an inhomogeneous spin linewidth of 16 kHz suitable for broadband magnetometry. Spin echoes on this sample showed a coherence time  $T_2$  in excess of several msec being limited by ambient magnetic field fluctuations. When

magnetic shielding is used, the lifetimes increase significantly and are too long to be measured with the current experimental setup.



**Figure 7. (a) Measured coherence time  $T_2^*$  for the NV electron spin in ultrapure  $^{12}\text{C}$  enriched diamond  $\sim 99.99\%$ . Width is  $1/(\pi T_2^*) \sim 16$  kHz.  $T_2^*$  is  $1/e$ , not  $1/2$ . (b) FFT showing 16 kHz spin linewidth. This is inhomogeneous width, which is much broader than homogeneous width.**

### Vector magnetometry using single NV defect electron spin

As mentioned before the NV is a vector magnetometer. The positions of the  $m_s=0 \leftrightarrow \pm 1$  spin resonances of a spin-1 system allow one to extract the magnitude of the local magnetic field and, under some approximations, the angle between the magnetic field and the symmetry axis of the system. The spin Hamiltonian of an  $S=1$  system having a distorted  $C_{3v}$  symmetry is given by the following expression:

$$H = \mu_B g \mathbf{B} \cdot \mathbf{S} + D \left( S_z^2 - S(S+1)/3 \right) + E \left( S_x^2 - S_y^2 \right),$$

where  $D$  and  $E$  are the zero-field splitting parameters,  $S=1$ ,  $\mu_B$  is Bohr magneton,  $g=2$  is the g-factor, and  $\mathbf{B}$  is the external magnetic field. The lack of axial symmetry reflected by the asymmetry parameter  $E$  unambiguously determines the natural local coordinate system with the z-axis being along the axis of the NV centre and x- and y-axes being along the principal axes of the distortion ellipsoid. In such a coordinate system, it is convenient to describe the magnetic field by its magnitude  $B$  and the two angles,  $\theta$  (polar) and  $\varphi$  (azymuthal). All parameters  $B$ ,  $\theta$ , and  $\varphi$  can be obtained from analysis of ESR spectrum. The positions of spin levels are given by the solutions of the characteristic equation:

$$x^3 - \left( \frac{D^2}{3} + E^2 + \beta^2 \right) x - \frac{\beta^2}{2} \left( D \cos 2\theta + 2E \cos 2\varphi \sin^2 \theta \right) - \frac{D}{6} \left( 4E^2 + \beta^2 \right) + \frac{2D^3}{27} = 0,$$

where  $\beta = \mu_B g B$ . Denoting the position of  $S_z = 0$  state as  $x_0$ , one finds that the positions of the  $S_z = \pm 1$  states are given by  $x_{\pm} = x_0 + v_{0\pm}$ , where  $v_{0\pm}$  are the experimentally measured frequencies of  $0 \leftrightarrow \pm 1$  spin transitions. Since  $x_{0,\pm}$  must satisfy the above mentioned equation, it is possible to obtain three equations for the four unknowns ( $x_0, B, \theta$ , and  $\varphi$ ) two of which,  $\theta$  and  $\varphi$ , form a unique combination

$\Delta = D \cos 2\theta + 2E \cos 2\varphi \sin^2 \theta$ . This set of equations gives the following solutions for  $\beta$  and  $\Delta$  :

$$\beta = \frac{1}{3}(\nu_1^2 + \nu_2^2 - \nu_1\nu_2 - D^2) - E^2,$$

$$\Delta = \frac{7D^3 + 2(\nu_1 + \nu_2)(2(\nu_1^2 + \nu_2^2) - 5\nu_1\nu_2 - 9E^2) - 3D(\nu_1^2 + \nu_2^2 - \nu_1\nu_2 + 9E^2)}{9(\nu_1^2 + \nu_2^2 - \nu_1\nu_2 - D^2 - 3E^2)}.$$

Since for NV centers  $D \gg E$ ,  $\Delta \approx D \cos 2\theta$ . Thus, knowing the zero-field splitting parameters and the frequencies of the  $0 \leftrightarrow \pm 1$  ESR resonances, one can find  $B$  and  $\theta$ . The solution of the inverse problem of finding the two ESR frequencies given the known  $B$  and  $\theta$  is presented in Figure 8. The upper (lower) branch corresponds to the transition  $0 \leftrightarrow +1$  ( $0 \leftrightarrow -1$ ).

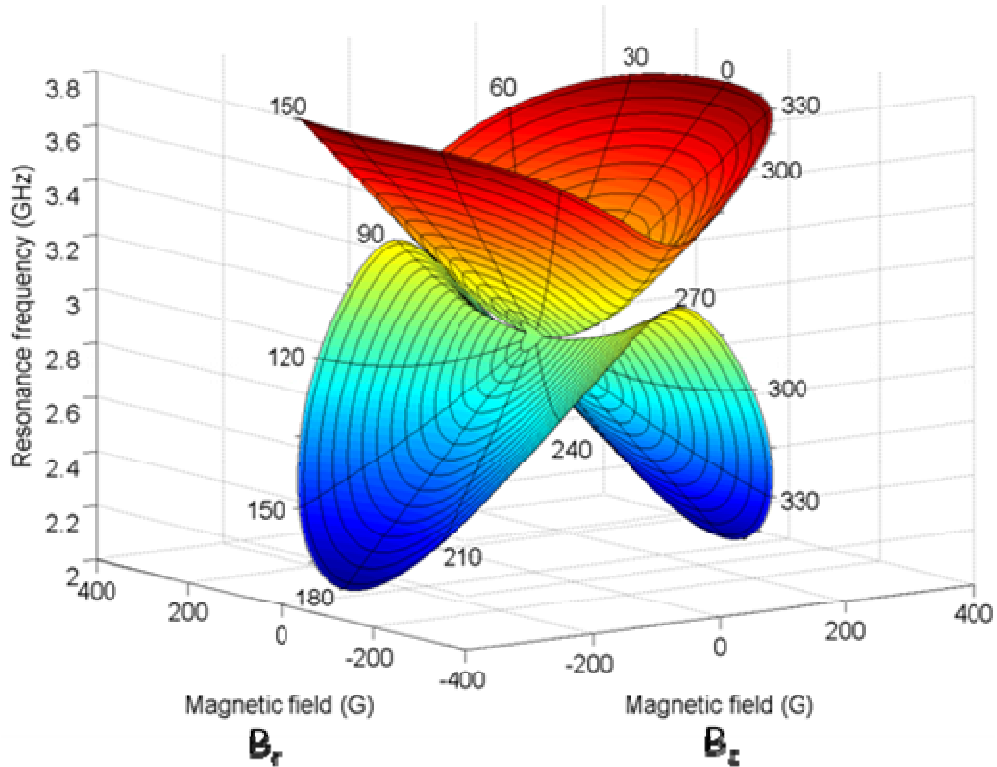
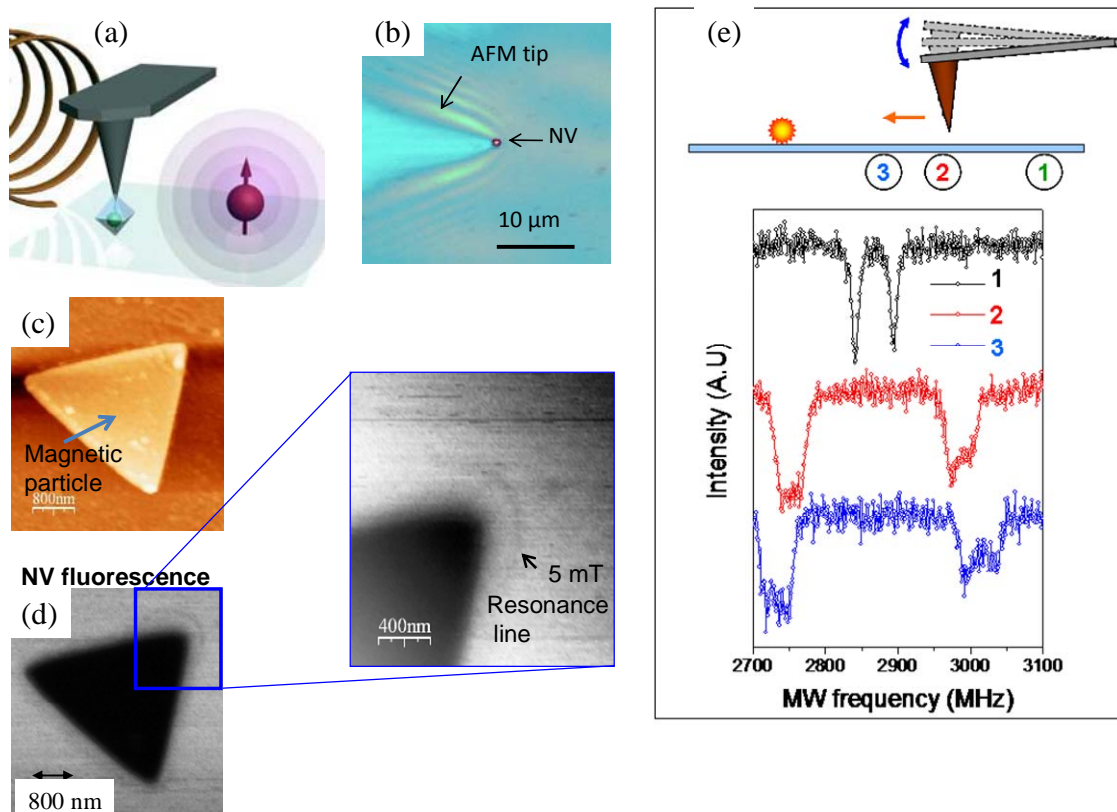


Figure 8. Dependence of ESR frequencies (GHz) on a magnetic field (kG) applied in different directions with respect to NV axis ( $0 \leq \theta \leq 2\pi$ ). The angle in respect to NV axis (in degrees) is indicated along resonant surface.

### Single NV magnetometers using diamond nanocrystal mounted to AFM tip

NV containing diamond nanocrystals were mounted to atomic force microscope (AFM) tips by a variety of techniques. These included UV curing epoxy, electrostatic forces, and capillary forces using micropipette tips. To demonstrate the feasibility of a scanning NV magnetometer we attached a nanocrystal containing a single NV on to the tip of a

cantilever, and used it to profile the magnetic field produced by a magnetic structure on nanometer length scales. The arrangement of the setup is shown in Figure 9a. Figure 9b shows a single NV attached to the AFM probe tip. Antibunching measurements verify that there is only one NV. Microwaves are tuned into resonance with the NV spin on the cantilever tip a particular distance from the magnetic particle. In the vicinity of the magnetic nanostructures the resonance condition is satisfied along well defined lines (iso-B contours) which serve to map out the spatial structure of the magnetic field. Figure 9c shows an optical image of a triangular magnetic structure fabricated by e-beam lithography using nickel. Figure 9d shows the fluorescence image obtained with single scanning NV defect as light source (as expected the magnetic particle appears as shadow in our detection geometry). The narrow dark line close to the corner represents space regions where the conditions for magnetic resonance of NV centre on the tip are fulfilled (marked spot in the inset corresponds to the magnetic value field of 45 G  $\sim$  5 mT). Note that image represents raw data acquired in just 4 minutes time. The magnetic field resolution is given by the width of the dark lines, which are about 20 nm. Taking into account the magnetic field gradient of 0.25 G/nm (measured by recording several resonance lines at different microwave frequencies, data not shown), it corresponds to a measurement accuracy of 5 G = 0.5 mT.



**Figure 9.** (a) Diagram of magnetic particles sensing with single NV defects fixed at the scanning probe tip. (b) Optical image of a diamond nanocrystal attached to an AFM tip (view from the bottom). Scattered light image of the tip is overlapped with the fluorescence image of the nanocrystal. Bright spot represents fluorescence of single NV defects. Fluorescence autocorrelation function (data not shown) shows a pronounced antibunching dip indicating a single NV defect in the nanocrystal. (c) Magnetic nickel nanostructure prepared by electron beam lithography. (d) Magnetic field imaging using the scanning probe single spin magnetometer. The image consists of the fluorescence signal of a

scanned NV centre attached to the apex of an AFM tip when resonant microwaves at 2750 MHz are applied (marked point in the inset corresponds to a 50 G magnetic field tilted by 45 degrees). (e) **Effect of vibrating cantilever on NV magnetometer signal near a micromagnet. The broadening of the spectral lines can be turned into an advantage by synchronizing an echo sequence with the vibration. In this way dc fields of nanomagnets can be detected using the more sensitive echo technique.**

One limiting factor here is oscillatory motion of the nanodiamond attached to the AFM tip. This is illustrated in Figure 9e where the spin transition linewidth broadens and distorts as the NV probe is brought closer to the magnetic nanoparticle. The resolution can be significantly improved by phase locking of the detection system to the oscillatory motion of the cantilever. When echo-based techniques with an echo period matched to a single oscillation period of the cantilever is employed and the AC instead of DC magnetic field is measured, the effective ESR linewidth is an inverse length of the free spin precession (100 kHz for standard AFM cantilevers). Hence we expect an improvement of field measurement accuracy by more than three orders of magnitude ( $3 \text{ mG} = 300 \text{ nT}$ ). For the magnetic field gradient caused by the structure imaged in Figure 9d this would result in a sub  $\text{\AA}$  spatial resolution

### **Fabricating diamond nanorods with single NVs**

The limiting magnetic sensitivity of scanning NV probes is relatively low, about 300 nT in the best NVs nanodiamonds seen so far. This is because nanocrystals are generally made from nitrogen-rich diamond which has short spin coherence times due to the NV magnetic interaction with the nitrogens. To overcome this problem, nanodiamonds can be fabricated by crushing ultrapure diamond. However, nitrogen would still need to be implanted otherwise none of the nanocrystals would have NVs. The other problem with crushing is that the strain and surface states introduced by the mechanical processing would cause decoherence. The surfaces of crushed diamond also have many surface states that could trap electrons that would also contribute to spin decoherence. To overcome these problems we investigated the possibility of fabricating NV probes using another technique, namely top-down nano-machining of diamond nanorods.

A top-down procedure was used to fabricate diamond nanowires from a bulk diamond crystal in this experiment (Figure 10). First, a resist layer was deposited on the diamond crystal and electron-beam lithography was used to define circular masks of diameters ranging from 100-250nm on the surface. An anisotropic etch was used to transfer the pattern into the crystal and realize straight wires of variable lengths ranging from 1-2 $\mu\text{m}$  with smooth sidewalls. Independent control over nanowire diameter and length allows for nanowires of different aspect ratios to be fabricated. The commercially available Type Ib diamond used in this experiment possess naturally existing NV centers that are distributed throughout the crystal, so that this technique results in random positioning of embedded NV centers in the nanowire cross section

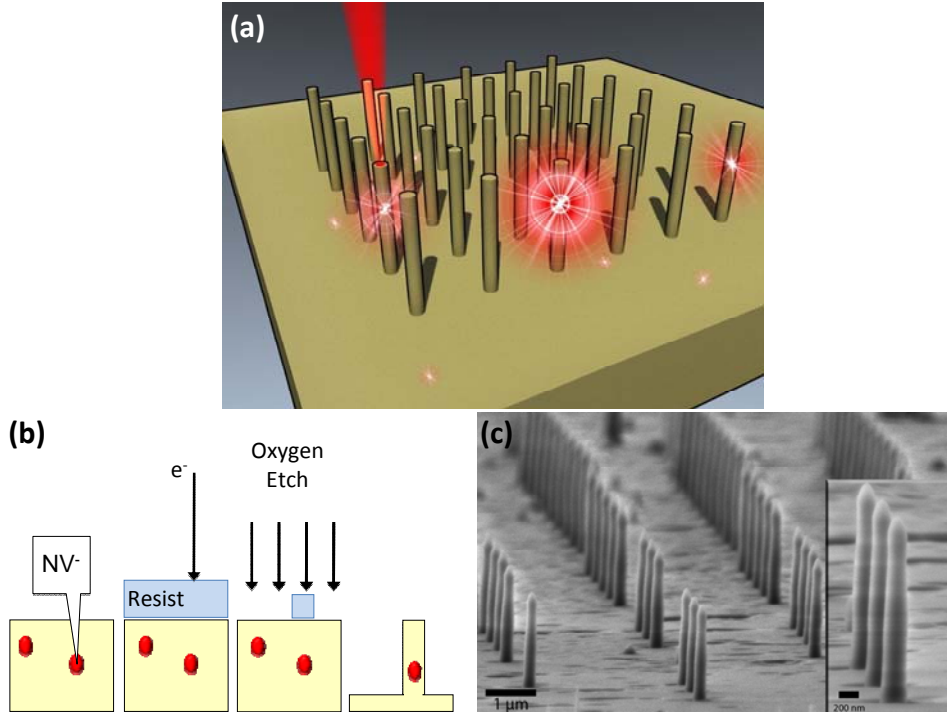


**Figure 10. Top-down Nanofabrication of a Diamond Wire with Individual Embedded NV Centers.** (a) By sculpting the dielectric environment around a NV center in a bulk diamond crystal, efficient channeling of single-photons to the waveguide mode can be used to facilitate photon collection. (b) Cartoon of the fabrication procedure utilized in this experiment, which involves e-beam lithography and RIE etching to generate diamond nanowires. (c) SEM micrograph of typical structures, which shows smooth side walls and slight tapering at the top facet.

The nanowire fabricated arrays were examined with a home-built room-temperature confocal microscope, which excites NV center fluorescence with a green (532nm) excitation laser and collects the NV center fluorescence. In this way, individual nanowires with high photon emission rates were easily identified from a scan of a device array (Figure 11b). The properties of these nanowire devices could be studied in detail for long periods of time (days) due to the mechanical stability of the diamond nanowire and photostability of the embedded NV center. Photoluminescence spectra of the photons emitted from the nanowire at room temperature show a zero-phonon line at 637nm with a phonon sideband from ~640-780nm. This confirms the presence of NV centers in the diamond nanowire device. The presence of an individual embedded NV center must be confirmed using a Hanbury Brown and Twiss Interferometer. This may be used to obtain the intensity autocorrelation function  $g^{(2)}(\tau) = \langle I(t)I(t + \tau) \rangle / \langle I(t) \rangle^2$ , which corresponds to a histogram of the time delay between consecutive photons emitted from the nanowire. The dramatic decrease in coincidence counts measured at zero delay ( $g^{(2)}(0) = 0.33$ ) results from the finite lifetime of the NV center excited state, and demonstrates the non-classical light emission from a single NV center in the nanowire (inset in Figure 11b).

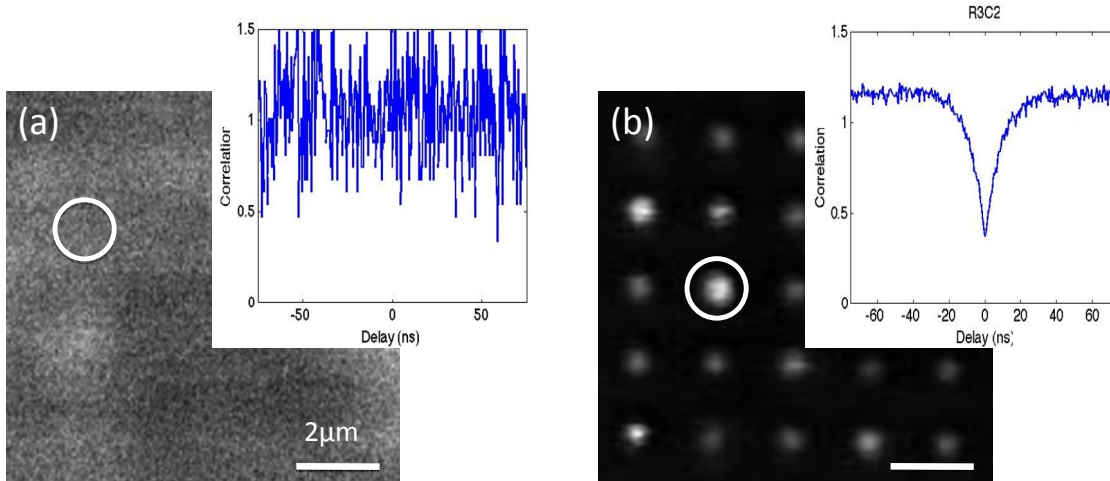


**Figure 11. Benefits of Nanostructuring for Single-Photon Emission. (a) Confocal microscope image of an unprocessed region of a single-crystal diamond. The system resolution is not sufficient to identify single NV centers. (b) Confocal microscope image of an array of wires. The combined effects of efficient single-photon generation and extraction allow for identification of single NV centers.**

As can be seen the fluorescence from a single NV is much brighter in the nanowire sample than in the original substrate (Figure 11a). Moreover, the photon emission rate from the NV center was fitted to the form  $I(P) = I_{\text{Sat}} P / (P + P_{\text{Sat}})$  and was observed to saturate at  $I_{\text{Sat}} \sim 370 \text{ kCPS}$  (counts per second) with  $P_{\text{Sat}} \sim 320 \mu\text{W}$  (Fig. 4b). Since the microscope system is filtering out 637nm-650nm photons, this gives a conservative estimate of  $\sim 1\%$  for the collection efficiency, which is a factor of ten improvement of single photon devices based on NV centers in bulk crystals and diamond nanoparticles using a similar air lens<sup>9</sup>. The brightness of the nanowire could be due to the coupling of multiple NV centers to the waveguide mode. Since the process of embedding NV centers in nanowire structures is random, it is possible that multiple NVs are embedded in the nanowire. However, the persistence of the photon antibunching indicates that the coupling between one NV and the waveguide mode dominates other background sources, including Raman scattering off of the diamond lattice, contributions from neutral NV centers.

We have demonstrated a technique for isolating individual color centers in single crystal diamond nanowires and realizing enhanced single photon collection. In the future, Nitrogen ion implantation techniques may be utilized to deterministically embed an NV center into the diamond nanowire and further improve single photon collection efficiency and spin lifetime. Moreover, fundamental studies of the properties of NV centers in nanowires, for example the zero-phonon transition, will facilitate their integration into more complex cavity structures with narrow linewidths for further enhancements.

### **Enhanced readout using repeated non-demolition read cycles**

The sensitivity of the NV magnetometer depends critically on how efficiently the spin state can be read out. Ideally a single readout shot would suffice. However, in practice hundreds of readouts must be performed to acquire a good enough signal to noise ratio.

Most of this is due to the fact that we normally only collect  $\sim 1\%$  of the NV fluorescence. The diamond nanowires promise to increase this significantly, and in fact the results so far suggest that in excess of 10% should be possible with optimized design. However, the fact that the fluorescence emission rate only differs by a factor of two means that we cannot achieve high fidelity single shot readout even for 100% fluorescence collection efficiency. To overcome this limitation we have examined the possibility of storing the spin information on a  $^{13}\text{C}$  nuclear spin the neighborhood of the NV. In the case of  $^{13}\text{C}$ -free diamond, the nuclear spin on a  $^{15}\text{N}$  nucleus which is part of the NV can be used instead. The basic idea is illustrated in Figure 12. Here Figure 12a shows a coupled NV and  $^{13}\text{C}$  spin system. The hyperfine interaction splits the NV  $m = 0 \rightarrow m = 1$  spin transition into two resolvable lines that are driven by microwave fields at MW1 and MW2, respectively. In addition a low frequency RF field is used to directly drive the nuclear spin transition in the  $m = -1$  electron state. As shown in Figure 12b the system is first optically polarized into the nuclear spin down sublevel of the  $m = 0$  electron state. This is done by first polarizing the electron to the  $m = 0$  state independent of nuclear spin. Then the population in the nuclear spin up sublevel of the  $m = 0$  electron state is transferred to the nuclear spin down sublevel of the  $m = 1$  electron state using sequential pi pulses at MW2 and RF. The optical polarization step is repeated and all population again ends up in the  $m = 0$  spin down state except that now it is only in the nuclear spin down sublevel.

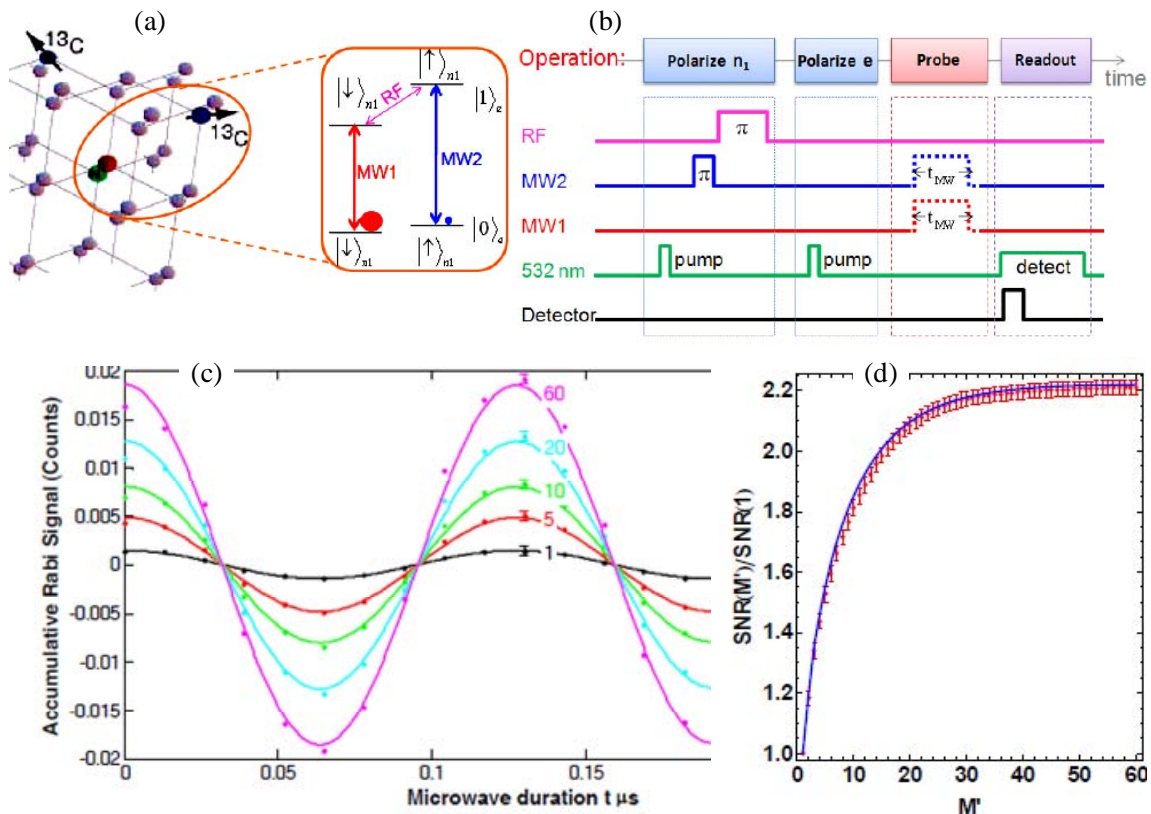


Figure 12. (a) Illustration of coupling between NV and nearby  $^{13}\text{C}$ . (b) Pulse sequence for transfer of electron spin coherence to nuclear spin and repetitive readout. (c) Cumulative Rabi signal obtained from repetitive readout, summed for 1; 5; 10; 20; 60 repetitions. The constant background counts are subtracted. (d) Improvement in the SNR using the repetitive readout scheme.

After interacting with a magnetic field the nuclear spin down sublevel of the electron spin  $m = 1$  state is transferred to the nuclear spin up sublevel of the  $m = 0$  sublevel by reversing the previous pulse sequence. Then either MW1 or MW2 are driven to selectively populate the electron  $m = 1$  state conditional on whether the nuclear spin down or up states are populated, respectively. Optical readout then attempts to determine if the electron  $m = 1$  state is populated or not by measuring the fluorescence count rate. After readout the population is back in the  $m = 0$  electron state but the nuclear spin state is preserved and so the process can be repeated many times to accumulate a better signal to noise ratio. The improvement in measurement contrast is shown in Figure 12c for up to 60 repetitions. The corresponding signal to noise ratio (SNR) is shown in Figure 12d. Compared to a single readout, the SNR is increased by 220%. The blue curve is simulation with imperfection parameters estimated from independent experiments.

If repetitive readout is combined with near 100% fluorescence collection efficiency then single shot readout should be possible. It should also be possible to optimize the repetitive readout by using coherent control techniques to suppress accidental excitation of both MW1 and MW2 transitions by only one of the fields.

### **Optimizing collection efficiency with plasmon wires**

Another promising technique to optimize the fluorescence collection efficiency for diamond nanocrystals is to use optical plasmons. Metallic nano-structures can have confined optical modes that are much smaller than the free space optical wavelength. This confinement leads to enhanced emission of spontaneous emission into the plasmon modes by the Purcell effect. This enhanced emission, combined with the fact that the plasmon mode can propagate several microns with relatively low loss, can potentially boost the NV enable very efficient fluorescent collection. To demonstrate this potential single NV colour centres in diamond nanocrystals were coupled to metallic waveguides, as shown in Figure 13. Crystalline, chemically grown silver wires were used as plasmon waveguides because of the low loss in silver in the visible spectral range. Nitrogen-vacancy emitters were placed in the near field of the nanowires by mixing a diamond nano-crystal solution with the silver wires, and spin-coating the resulting nanodiamond-coated wires onto a glass substrate. Figure 13a shows an atomic force microscopy image of diamond nanocrystals attached to the surface of a nanowire. Surprisingly, an efficient self-assembly process leads to sticking of single nanodiamond particles to wires. The inset shows the fluorescence image of the same wire with bright spots originating from emission of single nitrogen-vacancy defects. The size of diamond nanocrystals were about 50 nm and the average distance between emitter and metal is expected to be on the order of 25 nm. As a result of being placed in close proximity to the metallic surface, the nitrogen-vacancy defects show a significant reduction of their fluorescence lifetime owing to efficient coupling of the excited NV emission to surface plasmon polaritons. Enhanced decay rates of emitter due to excitation of surface plasmons are most important effect for distances between metal surface and NV centre within the range of 10-100 nm. Since the coupling is a near-field effect it depends on the distance between the surface of

the wire and each NV defect, and on the orientation of the NV emission dipole with respect to the axis of the wire.

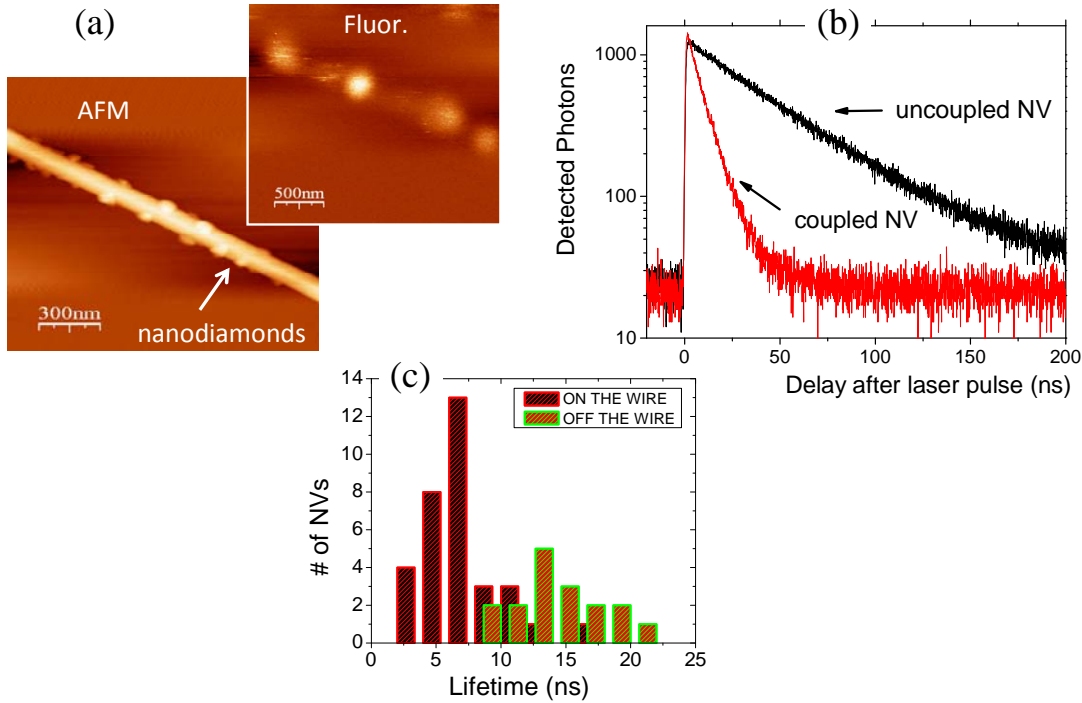


**Figure 13. (a) Atomic force microscopy image of diamond nanocrystals attached to a silver nanowire. Inset shows the fluorescence image of the wire with bright spots corresponding to the emission of single nitrogen-vacancy defects. (b) Fluorescence lifetime measurements of NV defects coupled to silver wire (red line) and isolated nanocrystals (black). (c) Distribution of fluorescence lifetimes for single NV emitters coupled to the wire showing an average Purcell factor of 2.5.**

The enhanced coupling is apparent from the enhanced decay rate for coupled NV seen in Figure 13b. Analysis of the Purcell factor for a number of different nanocrystals is shown in Figure 13c. On average we observe a Purcell factor of 2.5 which is in good agreement with the theoretically predicted value for an emitter-wire separation of 30 nm. In general, the coupling efficiency depends on the wire radius  $R$  as  $\frac{1}{R^3}$ , i.e. stronger coupling is expected for thinner wires. However, plasmon to photon conversion efficiency at the wire ends as well as plasmon propagation length increase with increasing  $R$ . Hence for the present experiment an average wire diameter of 70 nm was found to be a good compromise allowing efficient emitter coupling while keeping losses low and photon out-coupling high.

Although the NV emission is being efficiently coupled into the plasmon wires. The light propagating down the wires has yet to be efficiently coupled into our photon counters. To overcome this problem, coupling between plasmon wires and dielectric optical waveguides is being explored.

## Micron-scale applications

### Full frame imaging magnetometer for single neurons

In addition to magnetometry with single NVs. Ensembles of NVs might be capable of micron scale magnetic imaging of complex magnetic systems, for example neuron networks. An example of this is illustrated in Figure 14a. Here a 2-D magnetic field imager is constructed from a thin slab of NV diamond and a CCD camera. The magnetic fields produced by the 2-D magnetic source will give different Zeeman shifts at each location. If the NVs are excited with a microwave field near the electron spin resonance, then changes in the local field at each point in the source will produce changes in fluorescence collected from the correspond point on the NV diamond layer, which will then be imaged onto a single pixel of the CCD. The advantage of this full frame imaging technique over scanning probes is apparent if the magnetic field pattern changes rapidly with time. In the full frame imager this can be detected as changes in the fluorescence collected by all the CCD pixels in parallel in real time. The scanning probe technique would only be able to look at one point at a time and would miss all the complex 2-D interactions.

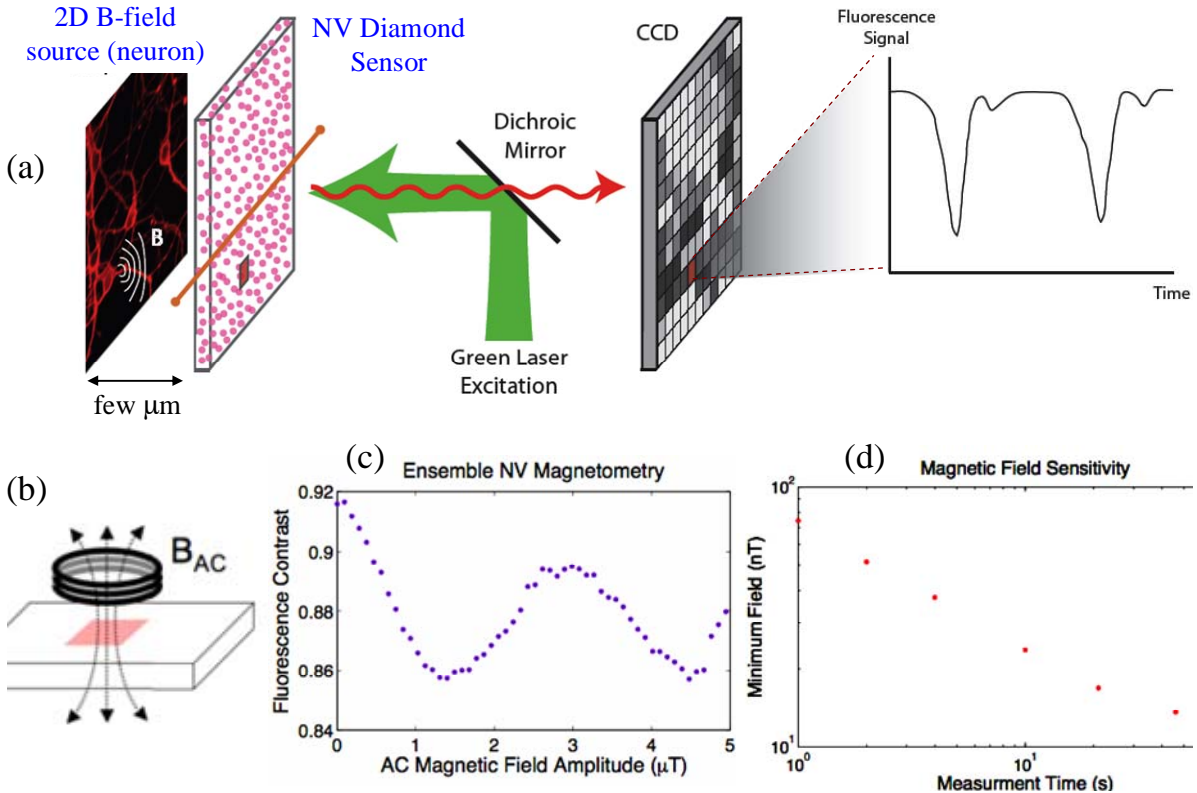
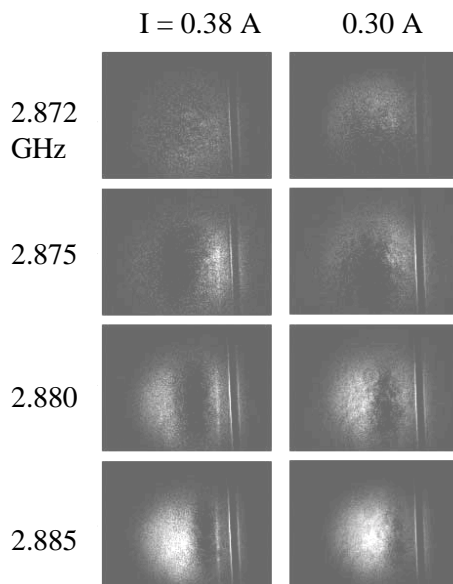


Figure 14. (a) Full frame magnetic imager. The magnetic object is within microns of a thin layer of NV centers which are excited by a microwave field (not shown). The fluorescent light is imaged onto a CCD. At each location the electron spin resonance occurs at a different frequency due to the Zeeman effect. If the magnetic field changes, the NVs at each location can move in and out of resonance producing changes in fluorescence. By simultaneous acquisition of full frame images, complex interdependences among magnet sources like neurons can be imaged. (b) Placement of the magnetic excitation coil to achieve a uniform AC magnetic field. (c) Fluorescence vs AC magnetic field amplitude for a uniform field. The signal is summed over many pixels (d) Corresponding magnetic sensitivity vs measurement time for the NV ensemble.

To demonstrate the full frame imaging concept the system is first configured to detect a uniform AC magnetic field using the CCD camera. This is done by first gating the camera so that the fluorescence is only integrated during the optical pumping time window. Then a spin echo sequence is applied to the NVs and the signal at each pixel is recorded. Summing over many pixels gives a sensitive measure of a uniform applied magnetic field as shown in Figure 14c. The corresponding magnetic sensitivity is  $\sim 80$  nT/sqrt(Hz) as shown in Figure 14d.

Full frame imaging is then demonstrated in Figure 15. Here current carrying wire oriented vertically is placed just above the NV doped diamond surface. When excited by a microwave field, the iso-magnetic field lines will appear as vertical dark stripes in the fluorescence. As either the microwave frequency or the current in the wire is changed the dark stripe will move horizontally. To enhance contrast the image acquired at a microwave frequency of 2.870 GHz was subtracted from the other images. As seen, the dark stripe is clearly visible and moves as expected. The narrow stripes on the right side of the images are due to the shadow of the wire. In this first demonstration, the magnetic resolution was low because cw microwave excitation was used. When the echo technique is applied, better performance is expected. However to achieve much higher magnetic resolution a thinner layer of NVs is needed. For this, a thin layer of nitrogen-rich CVD diamond will be grown on a fluorescence free substrate.



**Figure 15. The 2-D magnetic field near a wire is imaged with the full-frame magnetic imager. To improve contrast, the images shown are have been processed by subtracting the image obtained at a microwave frequency of 2.870 GHz which is relatively far off resonance with the microwave transition.**

**Summary of the most important results:**

Much better than expected magnetic sensitivity was achieved for single NV centers in isotopically pure bulk diamond. Significantly, the biggest improvement in sensitivity was achieved for broadband magnetic field detection, and this is important for many

applications. For both cw and ac magnetic fields the magnetic sensitivity of a single NV was so high that it required magnetic shielding. The main weakness is that multiple read cycles were needed to get a high signal to noise ratio because the magnetometer signal is superimposed on a fluorescence background. To achieve single-shot readout, the fluorescence collection efficiency must be greatly increased to at least 50% and the lifetime of the metastable level must be lengthened. To improve collection efficiency we examined diamond nanorods and plasmon optics with encouraging results, although more work is needed. To effectively increase the metastable lifetime we investigated storage of the information using long-lived nuclear spin states and applying multiple read non-demolition read cycles. This also showed encouraging results but more work is still needed to achieve the goal of digital readout. Finally, ensemble-based imaging magnetometer applications were explored using full frame CCD detection.